American Mineralogist, Volume 109, pages 1591–1597, 2024

First application of scintillator-based photon-counting computed tomography to rock samples: Preliminary results and prospects

Ayumi Ishiguro[1], Makoto Arimoto[1,2,3,4], Daichi Sato[1], Takahiro Tomoda[1], Keita Itano[5], Akihiro Tamura[3], Hironori Sugiyama[6], Takeshi Kawae[3], Mayuko Fukuyama[5], Jun Kataoka[4], Shinsuke Terazawa[7], Satoshi Shiota[7], and Tomoaki Morishita[3, 8,*]

[1]Graduate School of Natural Science & Technology, Kanazawa University, Kakuma, Kanazawa, Ishikawa 920-1192, Japan
[2]Advanced Research Center for Space Science and Technology, Kanazawa University, Kakuma, Kanazawa, Ishikawa 920-1192, Japan
[3]Institute of Science and Engineering, Kanazawa University, Kakuma, Kanazawa, Ishikawa 920-1192, Japan
[4]Faculty of Science and Engineering, Waseda University, 3-4-1, Okubo, Shinjuku, Tokyo 169-8555, Japan
[5]Graduate School of Engineering Science, Akita University, 1-1 Tegata-gakuen-machi, Akita 010-8502, Japan
[6]Instrumental Analysis Division, Engineering and Technology Department, Kanazawa University, Kakuma, Kanazawa, Ishikawa 920-1192, Japan
[7]Proterial Ltd, 2-15-17 Egawa, Shimamoto, Mishima, Osaka 618-0013, Japan
[8]Volcanoes and Earth's Interior Research Center, Japan Agency for Marine-Earth Science and Technology, 2-15 Natsushima, Kanagawa 237-0061, Japan

Abstract

Knowledge of the three-dimensional distribution of minerals in a rock sample is of fundamental importance to deciphering a sample's properties and history. Attenuation-contrast X-ray computed tomography (X-ray CT) is widely used in the geosciences to determine the three-dimensional distributions of minerals or pores, or both. Photon counting CT (PC-CT) uses a novel energy-resolved X-ray detector that allows X-rays with a continuous energy spectrum to be detected separately within arbitrary energy ranges. Here we report the first results of applying laboratory-build PC-CT combined with multi-pixel photon counter (MPPC) to common minerals such as quartz and calcite. In the low-energy range, PC-CT produced higher contrast images than single-energy X-ray CT. Minerals were successfully identified from the relationships between the mean CT values for each energy window and the mean difference between pairs of energy windows. These results suggest that PC-CT can produce high-contrast images of minerals and may be able to distinguish mineral phases with different attenuation curves, even when their CT values are similar. We obtained CT images of minerals in a natural sedimentary rock sample, composed mainly of quartz and carbonate. Although the spatial resolution of the detector in this study was insufficient for the sample, the main carbonate veins were clearly visible as high carbonate-content areas in the PC-CT images. Given some prior knowledge of mineral phases from other methods, it may be possible to use PC-CT imaging to obtain further information about their chemical compositions.

Keywords: Photon counting X-ray computed tomography, non-destructive testing tools for rocks

Introduction

Attenuation-contrast X-ray computed tomography (X-ray CT) allows us to observe the external and internal features of objects by analyzing differences in X-ray transmission between the different phases/materials composing the object. This technique has been widely used to determine three-dimensional distribution of minerals within the volumes of natural and artificial geomaterials using both laboratory-based and synchrotron-based X-ray sources (e.g., Ketcham 2005; Zandomeneghi et al. 2010; Voltolini et al. 2011; Baker et al. 2012; Cnudde and Boone 2013; Marinoni et al. 2015; Parisatto et al. 2018; Hibiya et al. 2019; Pak et al. 2019; Selem et al. 2021; Giamas et al. 2022). X-ray CT measures the linear attenuation coefficients, which are derived from differences in X-ray intensity before and after transmission. The linear attenuation coefficient is the total attenuation caused by the interaction of X-rays with a material, as the coefficient depends on the composition and density of the material. Materials composed of low atomic number elements have low linear attenuation values at the X-ray energies typically used for X-ray CT imaging (>40 keV). Single-energy X-ray CT imaging cannot easily observe the relationships among materials with similar compositions and densities, often composed of low atomic number elements (e.g., carbon, oxygen, and silicon). Dual-energy X-ray CT (DE-CT) has become established in recent years, especially in medicine (Mirzaei and Faghihi 2019; Schmidt and Flohr 2020). DE-CT uses two different data sets obtained at two energy levels (Odedra et al. 2022). The technique has also been applied to the Earth sciences (Sellerer et al. 2019; Martini et al. 2021; Hamm et al. 2022). However, DE-CT cannot adjust the applied energies to the specific requirements of a given imaging target in many cases, because the two tube voltages of the X-ray source are mostly fixed. As an energy-integrating detector is used for DE-CT, it is difficult to cut off or utilize X-rays in arbitrary energy regions. Attenuation coefficient changes in typical silicate rocks are enhanced in the low-energy range (e.g., 40–60 keV for

* Corresponding author E-mail: moripta@staff.kanazawa-u.ac.jp

0003-004X/24/0009–1591$05.00/DOI: https://doi.org/10.2138/am-2023-9099

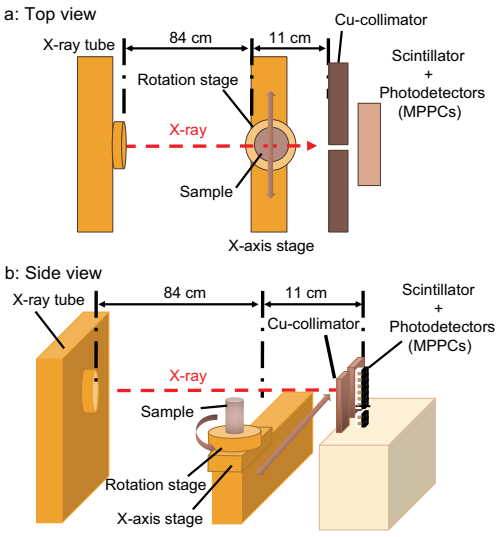

Figure 1. The laboratory-built photon counting computed tomography (PC-CT) system. (**a**) Top view. (**b**) Side view. (Color online.)

a sample of roughly a centimeter scale as in this study) compared to that in the high-energy range above ~80 keV. Thus, the use of an arbitrary X-ray energy band for X-ray CT imaging is crucial to investigate the spatial material distribution of low atomic number elements in rock samples, which is difficult for single energy-CT or for DE-CT.

Phase-contrast X-ray imaging that utilizes contrast changes caused by X-ray phase shift and refraction when X-rays pass through material (e.g., Davis et al. 1995; Momose 1995; Momose et al. 1996) is another powerful technique to better define the spatial distribution of constituents in geological materials, even in phases with weak absorption (Zandomeneghi et al. 2010; Moore et al. 2022).

Photon counting CT (PC-CT) uses a new technology based on an energy-resolved X-ray detector, which allows X-rays with a continuous energy spectrum to be detected separately in arbitrary energy regions (Willemink et al. 2018). Energy thresholds can be set to exclude noise (thus improving image quality) and to include any energy band within the total energy band available. The application of PC-CT to geomaterials is expected to remarkably improve discrimination of mineral phases in these samples. Sittner et al. (2021) was the first to apply a CT scanner equipped with a photon-counting line sensor, which is a cadmium telluride (CdTe) X-ray detector, to geologic materials containing heavy elements. They identified grains that may contain Au from the energy spectra. It is emphasized that this method was applied to material containing heavy elements with *K*-edge energies between 20 and 160 keV.

An innovative PC-CT that combines a multi-pixel photon counter (MPPC) with an extremely large signal gain (~10^6) and a very fast temporal response combined with a fast scintillator has been developed in our laboratory (Arimoto et al. 2018, 2023). This PC-CT system has already been applied to liquid or soft samples such as contrast agents and living organisms. Morita et al. (2017) used PC-CT images obtained only from low-energy signals to clearly distinguish between water and alcohol. The application of PC-CT has attracted attention as a clinical CT. Kiji et al. (2020), Sagisaka et al. (2023), and Sato et al. (2023) identified contrast agent phantoms and contrast agent material in mice. This paper examines and evaluates the feasibility of analyzing rock samples without materials with heavy elements using a laboratory-built PC-CT setup, expanding the application of the technique to diverse geomaterials.

Sample preparation and experimental methods

Sample preparation

We examined quartz (SiO_2, 2.5 g/cm^3) and calcite ($CaCO_3$, 2.71 g/cm^3), which are common minerals that often appear whitish in color on weathered surfaces and are sometimes difficult to distinguish with the naked eye.

Samples were prepared from single crystals of each mineral. Cylinders of 7.6 mm diameter were cored using a drill core to maintain a constant transmission of X-rays as the samples were rotated during CT analysis. The core size used here (~8 mm) was determined through preliminary experiments to suppress beam-hardening artifacts in the CT images; the results of our previous preliminary experiments show that the CT images of rocks with a thickness of ~50 mm or more exhibit a severe beam-hardening artifact. Rocks with a thickness of 10 mm or less showed no significant beam-hardening artifacts when using X-ray photon energies above 40 keV. Therefore, we utilized X-ray photon energies above 40 keV, and no correction for beam-hardening artifacts was performed in this study. The quartz was drilled perpendicular to the C-axis, and the calcite was drilled perpendicular to a cleavage plane.

Experimental conditions

X-rays were generated using an industrial X-ray tube (RXG-2059, R-TEC Co. Ltd.) with a maximum tube voltage and current of 150 kV and 0.5 mA, respectively. The generated X-rays passed through the object to be imaged and were detected using a 64-channel ceramic scintillator array (yttrium-gadolinium-aluminum-gallium garnet) with a voxel size of 1 × 1 × 1 mm^3 coupled to a 64-channel multi-pixel photon counter (MPPC) array with a pixel size of (1 × 1) mm^2 (Hamamatsu Photonics) (Figs. 1a and 1b). Current signals from the MPPCs were processed using a newly developed 64-channel large-scale integrated circuit (LSI) (Arimoto et al. 2023). The chip's gain correction capability could compensate for the MPPC response, and its digital-to-analog converters could set precise threshold voltages (i.e., energies) to compensate for intrinsic variation due to the LSI production process. The energy resolution was estimated to be 40.5% full-width at half maximum based on Gaussian fitting of the measured ^{241}Am spectra of each channel at 59.5 keV. The maximum countable count rate of 1/(250 ns), ~4 MHz, was estimated from the relation between the photon counting rate above 23 keV and the tube current, and the dead time obtained by fitting with the non-extended dead time model (Arimoto et al. 2023). As shown in Figure 1a, the detector is always positioned along the central axis of the X-ray beam, and this system's geometry can be considered as a parallel beam. Therefore, a filtered back projection (FBP) was used for image reconstruction. The collimator was used to prevent scattering of the X-ray photons. The spatial resolution was 0.25 × 0.25 × 0.8 mm; the *x*- and *y*-axis spatial resolution of 0.25 mm, which is much smaller than the detector pixel size of 1 mm, is determined by the fact of translating the detector perpendicular to the direction of the incident X-ray beam using a 0.25-mm increment. The *z*-axis spatial resolution is determined by the magnification effect: the X-ray beam diverges as a cone from the source to irradiate the target object and reaches the detector. The magnification factor is calculated to be 0.8 by considering the geometric positions of the source, target object and the detector. The experimental conditions were as follows: X-ray source at 120 kV and 0.1 mA, 1.5 mm aluminum filter, 400 ms exposure time, and six measured energy bands of 40–50, 50–60, 60–70, 70–85, 85–95, and >95 keV. Note that a 1.5 mm aluminum filter was applied to decrease the X-ray flux in the low-energy range (<50 keV) and mitigate the pulse pile-up effect in a single pixel. Table 1 shows the analytical conditions for this experiment. Kiji et al. (2020) reported details of the analysis procedure.

Results

CT values vs. energy

The experimental results on virtual sections at different energies in Figures 2 and 3 were reconstructed from CT values. CT

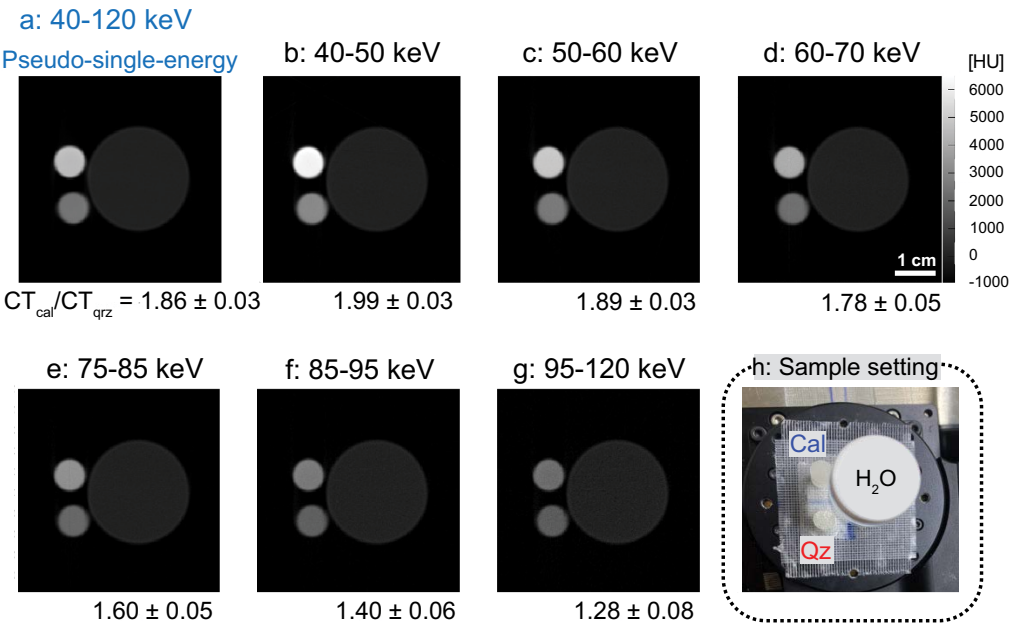

FIGURE 2. CT images acquired using the full energy range of 40–120 keV (**a**), and six different energy windows (**b**–**g**). Sample setup is also shown (**h**). The image from using the full energy range is a pseudo-single-energy CT image. Increasing brightness indicates increasing CT values, as quantified by the grayscale bar on the right of **d**. HU = CT value with the Hounsfield unit. The ratio of the CT values of calcite and quartz (CT_{cal}/CT_{qtz}) for each image is shown below each one (**a**–**g**). In each panel, the upper small circle is calcite, the lower small circle is quartz, and the large circle is water. (Color online.)

values expressed as the Hounsfield unit (*CT*) were obtained from linear attenuation coefficients of the samples normalized by that of water in each analysis, thereby eliminating the influence of the analytical conditions., and were normalized following Equation 1.

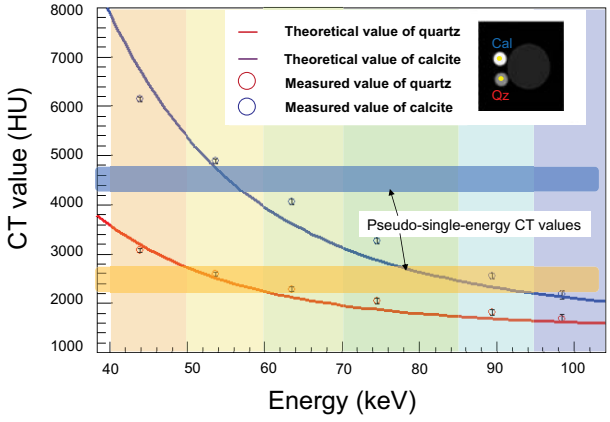

FIGURE 3. Relationship between photon energy and CT value. Red and blue open circles are CT values for quartz and calcite, respectively, measured using the six energy windows shaded orange (40–50 keV), yellow (50–60 keV), light green (60–70 keV), green (70–85 keV), light blue (85–95 keV), and light purple (95–120 keV). HU = CT value with the Hounsfield unit. Red and blue solid lines are theoretical CT values for quartz and calcite, respectively, derived using ideal linear attenuation coefficients from the NIST database (https://physics.nist.gov/PhysRefData/Xcom/html/xcom1.html). Light orange and light blue bands show the CT values for quartz and calcite, respectively, from pseudo-single-energy CT (using the 40–120 keV range). See the text for details. (Color online.)

$$CT = 1000(\mu - \mu_w)/\mu_w \quad (1)$$

where μ is the linear attenuation coefficient of the sample, and μ_w is that of water. The CT value of water is thus 0, and that of air is –1000.

The linear attenuation coefficient is the product of the mass attenuation coefficient (μ′) and density (ρ):

$$\mu = \rho\mu'. \quad (2)$$

Therefore, the density of a known mineral can be verified independently using the measured CT values. This could be useful for confirming the identity of the mineral. Density estimation from PC-CT values is a powerful tool for estimating the concentrations of target elements in solution (Kiji et al. 2020). For solid samples of known composition, properties such as porosity can be estimated from the density obtained using PC-CT.

Figure 2 shows CT images obtained using six different energy windows. The low-energy regions feature higher measured CT values than the high-energy ones (Fig. 3), as evidenced by the trend of the images darkening as the X-ray photon energy increased. This indicates that the six different images reflect the relationship between X-ray energy and attenuation. The measured CT values were almost consistent with the theoretical ones derived from Equation 1 using the ideal linear attenuation coefficients from the NIST database (https://physics.nist.gov/PhysRefData/Xcom/html/xcom1.html). However the measured CT values slightly deviate from the theoretical values, probably because the beam hardening effect is more pronounced at the lower energies with a broad energy window of approximately 10 keV or more.

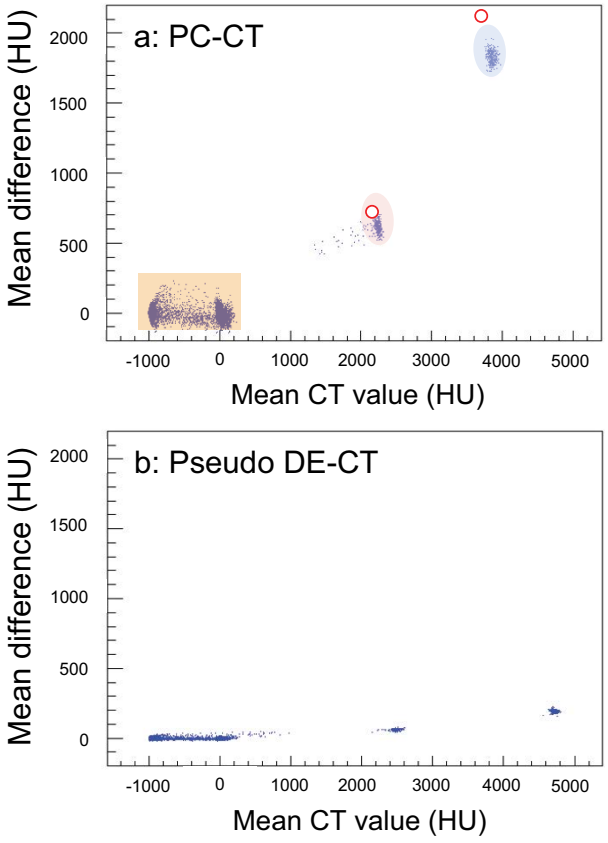

FIGURE 4. Relationship between mean CT values (Mean CT) and the mean of the differences between CT values obtained using different pairs of energy windows (Mean Diff) (**a**), and two energy regions (40–75 and 40–60 keV) (**b**). HU = CT value with the Hounsfield unit. Blue dots are all the pixels in the CT image. Red open circles in **a** are ideal values for calcite and quartz. The orange area in **a** is the mixture of water (CT value around 0) and air (CT value around –1000). Red and blue areas in **a** represent the CT ranges of quartz and calcite, respectively, at the spatial resolution of this study (i.e., the deviations from the main cluster represent a mixture of each material and the surrounding material such as air). Data (**b**) obtained from the broader energy range (40–75 keV) are essentially identical to DE-CT results obtained from the same energy range ("pseudo- DE-CT" in the text). (Color online.)

DISCUSSION

Single-energy X-ray CT vs. PC-CT imaging

Images and data from the lowest-energy window (40–50 keV) were compared with images and data obtained in the full energy range (40–120 keV), which corresponds approximately to single-energy X-ray CT results (and is thus referred to here as pseudo-single-energy CT; Fig. 2). The ratios of the CT values of calcite to quartz (CT_{cal}/CT_{qtz}) at different energies are shown in Figure 2. These values show that the ratio of CT_{cal}/CT_{qtz} becomes higher at lower energy. Similarly, Figure 3 shows that the differences between the CT values (theoretical and measured) for quartz and calcite are greatest at low energy.

Figures 2 and 3 suggest that using the low-energy window gives a larger ratio of the two CT values (i.e., the contrast is higher) than when using pseudo-single-energy X-ray CT. Therefore, data obtained using a low-energy window can be used to clearly identify mineral phases.

Mineral distribution mapping

This section discusses the potential of PC-CT to identify and display the spatial distribution of a particular mineral. Single-energy X-ray CT and DE-CT have also successfully identified several minerals (Arif et al. 2021; Martini et al. 2021) using only information obtained from the whole energy range or two energy windows. In comparison, the use of multiple energy windows in PC-CT may provide more information on each mineral. Kiji et al. (2020) showed that PC-CT can estimate the concentrations in solution of contrast agents such as iodine and gadolinium. However, many minerals such as quartz and calcite do not have *K*-edges in the X-ray energy range used by PC-CT (about 30–120 keV). Therefore, this study referred to the approach of Alessio and MacDonald (2013) for characterizing materials that do not have *K*-edges in the observed X-ray energy range. Phases are classified using the relationships between the mean of the CT values for each energy window (Mean CT; Eq. 3) and the mean of the difference in CT values between any two energy windows (Mean Diff; Eq. 4):

$$\text{Mean CT} = \frac{\sum_{n=0}^{E} CT_n}{E} \tag{3}$$

$$\text{Mean Diff} = \frac{\sum_{e2=0}^{E}\sum_{e1=1}^{E}\left(CT_{e1} - CT_{e2}\right)}{E\left(E-1\right)/2} \tag{4}$$

where CT_n is the CT value of each energy window, $CT_{e1} - CT_{e2}$ is the difference between the CT values of energy windows $e1$ and $e2$, and E is the number of energy windows ($E = 6$ for this study). As Mean CT is the average of the CT values for each energy window, its value depends on the density and linear attenuation coefficient, and it is larger for denser and heavier components. As Mean Diff is the average difference of the CT values for any two energy windows, a larger value indicates a steeper slope of the attenuation curve. Therefore, this value depends on the change in energy of the linear attenuation coefficient, which is determined by the attenuation curve. In general, materials containing heavier constituents have a steeper attenuation curve, which results in larger average differences.

Figure 4 shows the relationships between the mean difference and the mean CT values for all pixels obtained from PC-CT images of calcite and quartz cylinders. The data form four clusters in three regions (blue, orange, and pink). The clusters with high Mean Diff and high Mean CT are consistent with the theoretical values for quartz and calcite at each energy range (red circles). Both the Mean CT and Mean Diff data can vary, even for homogeneous materials, probably due to counting statistics and the fact that CT reconstruction algorithm inherently amplifies statistical noise and other systematic uncertainties. The variation of the data points in three shaded regions were interpreted as representing a mixture of each mineral and air.

The MPPC-CT data for each pixel were then used for identification of the minerals in each pixel. In Figure 4, we selected an area containing pixels representing the same type of mineral. Only pixels representing the same type of mineral are displayed in Figure 5. Here, the identification of minerals requires the following assumptions: candidates for the main constituent minerals

in the target sample are given as preliminary information (i.e., quartz or calcite in this figure), and each pixel represents only one mineral. Given data deviations, values with a deviation within ~200 HU from the median Mean CT and Mean Diff values in Figure 4 are assumed to be from the same mineral.

Comparison of energy information between DE-CT and PC-CT

We compare energy information between PC-CT using six energy bands and pseudo-DE-CT using two energy windows (40–60 and 40–75 keV). We mimic the DE-CT system by using two energy bands with our PC-CT system for comparing different systems with the same X-ray source. Figure 4 shows the relationship between Mean CT and Mean Diff for data obtained from the two pseudo-DE-CT energy regions compared to data from the six energy bands. It should be emphasized that the mean difference (the *y* axis in Fig. 4) is significantly wider for PC-CT than for pseudo-DE-CT. The plotted mean difference in CT values for each energy window indicates differences in the slope of the attenuation curve of each material, with a larger slope correlating with a larger mean difference. The mean CT values for quartz and calcite are different enough to identify each phase without using the Mean Diff values. However, if two materials with similar CT values have different attenuation curves (e.g., high atomic number material with a low density and low atomic number material with a high density), the PC-CT has a great potential to identify minerals with similar CT values. Furthermore, the advantage of PC-CT stands out when identifying more than three phases in the same sample.

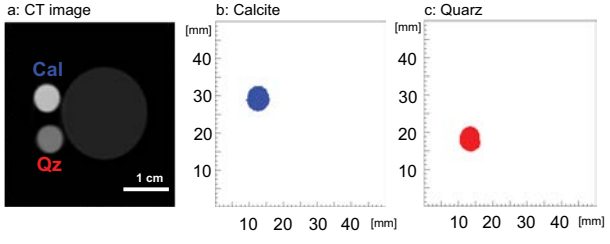

FIGURE 5. Semi-automatic identification of calcite (blue, middle) (**b**) and quartz (red, right) (**c**) from a representative CT image in the 40–120 keV window (**a**) by using the mean CT – mean difference plane shown in Figure 4. (Color online.)

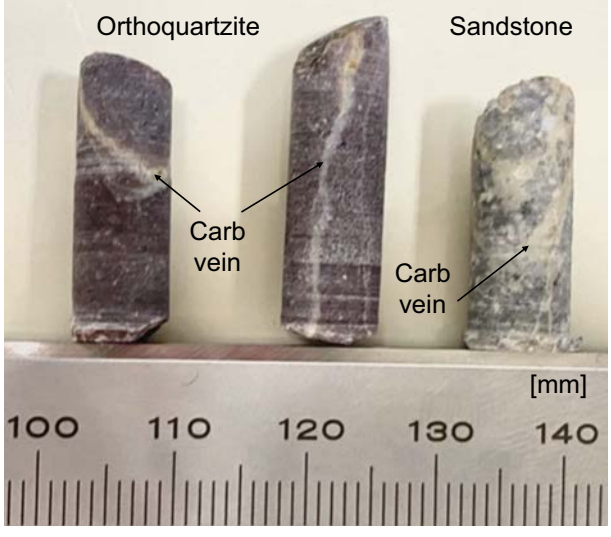

FIGURE 6. Samples of sandstone (right) and two orthoquartzite (left and middle) cores with carbonate veins (white millimeter-scale veins). (Color online.)

Example application of MPPC-CT to natural rock samples

Samples of sandstone and orthoquartzite from the Tetori Group, Ishikawa Prefecture, Japan, were treated as unknown samples. Their main constituent minerals were known to be mainly quartz grains cemented with carbonate minerals and cut by white veins dominated by carbonate (Kim et al. 2007) (Fig. 6; Online Materials[1] Figs. A1 and A2).

Figure 7 shows CT images acquired using six different energy windows. Theoretical CT values for quartz and calcite were compared with the values measured for orthoquartzite and carbonate-dominated veins (Fig. 8). The CT values measured for quartz were close to the theoretical values, but the values measured for the cement in the quartz-rich area and carbonate veins were much lower than the theoretical values for calcite (Fig. 8). The detector used here had a pixel size of ~1 mm. The lower-than-ideal calcite values may have been due to the calcite signals mixing with those from other minerals (mainly quartz) in these samples. Thin sections were prepared from the samples and observed using an optical microscope and a secondary electron microscope at Kanazawa University (see Online Materials[1] Fig. A2). Carbonate minerals were present in the carbonate veins and in the matrix around the quartz. Carbonate veins were not pure carbonate but contained many small SiO_2 phases. As most

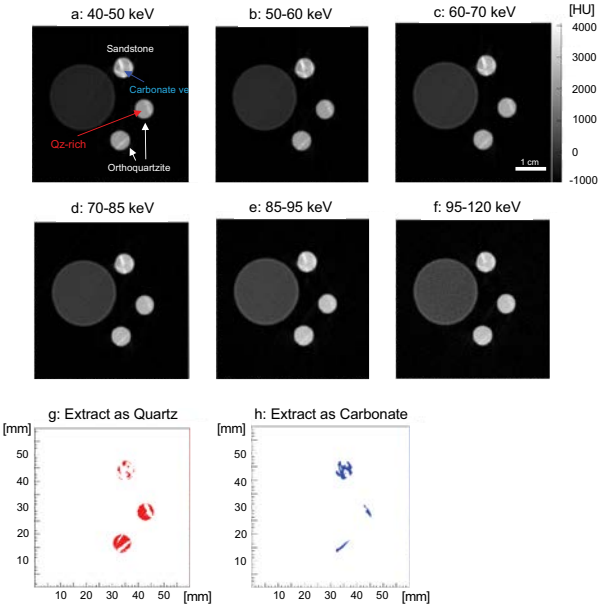

FIGURE 7. CT images of sedimentary rocks (small circles) and water (large circle) acquired using six different energy windows (**a**–**f**). The grayscale bar on the right of **c** indicates the CT value. The distributions of quartz (red) (**g**) and carbonate (blue) (**h**) obtained using the same method as in Figure 5 are also shown. (Color online.)

Table 1. Experimental setup for photon counting-CT imaging

Sample	Sample A (minerals)	Sample B (Tetori Formation)
X-axis movement step/total amount (mm)	0.25/50	0.25/60
CT rotation angle step/total amount (°)	1.125/180	0.9375/180
Number of projections	160	192
Exposure time for each projection (ms)	400	700
Tube voltage/current (kV/mA)	120/0.1	120/0.2
Energy threshold (keV)	40–50, 50–60, 60–70, 70–85, 85–95, and >95 keV	40–50, 50–60, 60–70, 70–85, 85–95, and >95 keV

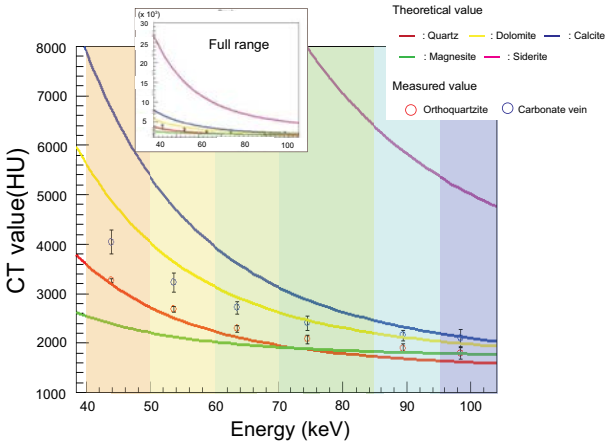

Figure 8. Relationship between photon energy and CT value. HU = CT value with the Hounsfield unit. Red and blue open circles are CT values for the matrix and the white millimeter-scale carbonate vein of one quartzite sample, respectively, measured using six energy windows shown as orange (40–50 keV), yellow (50–60 keV), light green (60–70 keV), green (70–85 keV), light blue (85–95 keV), and light purple (95–120 keV). Red, purple, blue, yellow, and green solid lines are theoretical CT values for quartz (SiO_2), siderite ($FeCO_3$), calcite ($CaCO_3$), dolomite [$CaMg(CO_3)_2$] and magnesite ($MgCO_3$), respectively. (Color online.)

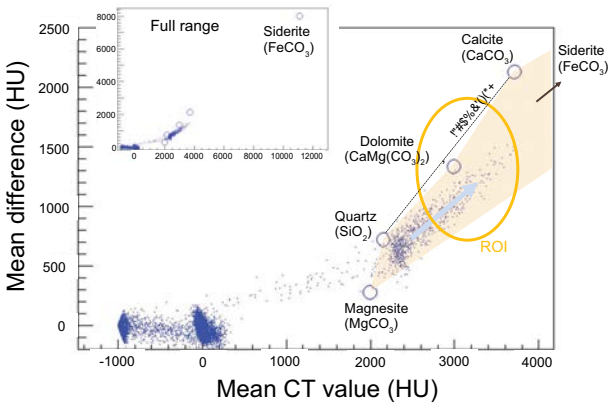

Figure 9. Relationship between mean CT values (Mean CT) and the mean of differences in CT values (Mean Diff). HU = CT value with the Hounsfield unit. Blue dots represent all pixels in the CT image. Blue open circles are ideal values for carbonate minerals (calcite, dolomite, magnesite, and siderite) and quartz. The orange area represents the CT ranges for mixtures of quartz and carbonate minerals. Yellow circle is the region of interests (ROI) indicated by a radius of 600 HU (dimensionless CT value with the Hounsfield unit) centered on the mean value of Mean CT and Mean Diff values for the carbonate vein. (Color online.)

calcite grains in both the veins and matrix were <1 mm in size, the measured value was most likely composed of mixed signals from quartz and carbonate.

It is interesting that the measured values for carbonate veins appear to deviate systematically from the ideal calcite values (Fig. 8). The major component of the carbonate minerals determined using scanning electron microscope equipped with energy-dispersive X-ray spectrometry (SEM-EDS) in these samples is dolomite with $FeCO_3$, rather than calcite (see Online Materials[1] Table A1 and text). In fact, the CT values measured for carbonate veins in the samples were close to the ideal CT value for dolomite (Fig. 8). This is consistent with previous studies of sedimentary rocks of the Tetori Formation (e.g., Kim et al. 2007). The systematic deviation from the ideal mixing of quartz and calcite (dashed line in Fig. 9) was likely caused by differences in the chemical composition of the carbonate.

Although these factors prevented pure calcite values from being obtained, plotting only the region of interests (ROI) indicated by a yellow circle of radius of 600 HU (dimensionless CT value using Hounsfield units) centered on the mean value of Mean CT and Mean Diff values for the carbonate vein in Figure 9 can clearly visualize the main calcite vein as a high-carbonate area in the PC-CT sections (Fig. 7).

Implications

This paper reports a laboratory-built PC-CT system and the first application of PC-CT for the non-destructive observation of quartz and calcite. Measured CT values for these minerals agreed well with theoretical values. Our results suggest that PC-CT has the potential to distinguish mineral phases with different attenuation curves, even for minerals with similar CT values. In addition, information on chemical composition can be obtained using PC-CT if the target mineral can be estimated by other methods. Applying a powerful X-ray source and detector with improved pixel size may make PC-CT more useful than single-energy X-ray CT and DE-CT methods for identifying the distributions of minerals in rock samples.

Acknowledgments and Funding

We thank Susumu Umino and Tomoyuki Mizukami for discussing this study. Valuable comments by Mark Rivers and an anonymous reviewer and suggestions from the editor greatly improved the revised manuscript. This study was financially supported by a Grants-in-Aid for Scientific Research from the Ministry of Education Culture, Sports, Science and Technology of Japan (no. JP20K20941 to T.M. and no. JP19H04483 to MA), JST ERATO Grant number JPMJER2102 to M.A. and J.K. and the Mitani Foundation for Research and Development 2020 to T.M. and M.A.

Referenced Cited

Alessio, A.M. and MacDonald, L.R. (2013) Quantitative material characterization from multi-energy photon counting CT. Medical Physics, 40, 031108, https://doi.org/10.1118/1.4790692.

Arif, M., Mahmoud, M., Zhang, Y., and Iglauer, S. (2021) X-ray tomography

imaging of shale microstructures: A review in the context of multiscale correlative imaging. International Journal of Coal Geology, 233, 103641, https://doi.org/10.1016/j.coal.2020.103641.

Arimoto, M., Morita, H., Fujieda, K., Maruhashi, T., Kataoka, J., Nitta, H., and Ikeda, H. (2018) Development of LSI for a new kind of photon-counting computed tomography using multipixel photon counters. Nuclear Instruments and Methods in Physics Research Section A: Accelerators, Spectrometers, Detectors and Associated Equipment, 912, 186–190, https://doi.org/10.1016/j.nima.2017.11.031.

Arimoto, M., Sato, D., Mizuno, T., Yoshiura, K., Ishiguro, K., Tomoda, T., Kawashima, H., Kobayashi, S., Kataoka, J., Sagisaka, M., and others. (2023) Development of 64-channel LSI with ultrafast analog and digital signal processing dedicated for photon-counting computed tomography with multi-pixel photon counter. Nuclear Instruments and Methods in Physics Research Section A: Accelerators, Spectrometers, Detectors and Associated Equipment, 1047, 167721, https://doi.org/10.1016/j.nima.2022.167721.

Baker, D.R., Mancini, L., Polacci, M., Higgins, M.D., Gualda, G.A.R., Hill, R.J., and Rivers, M.L. (2012) An introduction to the application of X-ray microtomography to the three-dimensional study of igneous rocks. Lithos, 148, 262–276, https://doi.org/10.1016/j.lithos.2012.06.008.

Cnudde, V. and Boone, M.N. (2013) High resolution X-ray computed tomography in geosciences: A review of the current technology and applications. Earth-Science Reviews, 123, 1–17, https://doi.org/10.1016/j.earscirev.2013.04.003.

Davis, T.J., Gao, D., Gureyev, T.E., Stevenson, A.W., and Wilkins, S.W. (1995) Phase-contrast imaging of weakly absorbing materials using hard X-rays. Nature, 373, 595–598, https://doi.org/10.1038/373595a0.

Giamas, V., Koutsovitis, P., Sideridis, A., Turberg, P., Grammatikopoulos, T.A., Petrounias, P., Giannakopoulou, P.P., Koukouzas, N., and Hatzipanagiotou, K. (2022) Effectiveness of X-ray micro-CT applications upon mafic and ultramafic ophiolitic rocks. Micron, 158, 103292, https://doi.org/10.1016/j.micron.2022.103292.

Hamm, C.A., Hampe, O., Mews, J., Günter, C., Milke, R., Witzmann, F., Savic, L.J., Hecht, L., Meister, S., Hamm, B., and others. (2022) Quantitative dual-energy CT as a nondestructive tool to identify indicators for fossilized bone in vertebrate paleontology. Scientific Reports, 12, 16407, https://doi.org/10.1038/s41598-022-20707-5.

Hibiya, Y., Archer, G.J., Tanaka, R., Sanborn, M.E., Sato, Y., Iizuka, T., Ozawa, K., Walker, R.J., Yamaguchi, A., Yin, Q.Z., and others. (2019) The origin of the unique achondrite Northwest Africa 6704: Constraints from petrology, chemistry and Re-Os, O and Ti isotope systematics. Geochimica et Cosmochimica Acta, 245, 597–627, https://doi.org/10.1016/j.gca.2018.04.031.

Ketcham, R.A. (2005) Computational methods for quantitative analysis of three-dimensional features in geological specimens. Geosphere, 1, 32–41, https://doi.org/10.1130/GES00001.1.

Kiji, H., Maruhashi, T., Toyoda, T., Kataoka, J., Arimoto, M., Sato, D., Yoshiura, K., Kobayashi, S., Kawashima, H., Terazawa, S., and others. (2020) 64-channel photon-counting computed tomography using a new MPPC-CT system. Nuclear Instruments and Methods in Physics Research Section A: Accelerators, Spectrometers, Detectors and Associated Equipment, 984, 164610, https://doi.org/10.1016/j.nima.2020.164610.

Kim, Y., Lee, Y.-I., and Hisada, K.-I. (2007) Provenance of quartzarenite clasts in the Tetori Group (Middle Jurassic to Early Cretaceous), Japan: Paleogeographic implications. Journal of Asian Earth Sciences, 29, 116–126, https://doi.org/10.1016/j.jseaes.2006.01.005.

Marinoni, N., Voltolini, M., Broekmans, M.A.T.M., Mancini, L., Monteiro, P.J.M., Rotiroti, N., Ferrari, E., and Bernasconi, A. (2015) A combined synchrotron radiation micro computed tomography and micro X-ray diffraction study on deleterious alkali-silica reaction. Journal of Material Science, 50, 7985–7997, https://doi.org/10.1007/s10853-015-9364-7.

Martini, M., Francus, P., Di Schiavi Trotta, L., and Després, P. (2021) Identification of common minerals using stoichiometric calibration method for dual-energy CT. Geochemistry, Geophysics, Geosystems, 22, e2021GC009885.

Mirzaei, F. and Faghihi, R. (2019) Quantification of contrast agent materials using a new image- domain multi material decomposition algorithm based on dual energy CT. BJR|Open, 1, 20180008.

Morita, H., Oshima, T., Kataoka, J., Arimoto, M., and Nitta, H. (2017) Novel photon-counting low-dose computed tomography using a multi-pixel photon counter. Nuclear Instruments and Methods in Physics Research Section A: Accelerators, Spectrometers, Detectors and Associated Equipment, 857, 58–65.

Momose, A. (1995) Demonstration of phase-contrast X-ray computed tomography using an X-ray interferometer. Nuclear Instruments and Methods in Physics Research Section A: Accelerators, Spectrometers, Detectors and Associated Equipment, 352, 622–628, https://doi.org/10.1016/0168-9002(95)90017-9.

Momose, A., Takeda, T., Itai, Y., and Hirano, K. (1996) Phase-contrast X-ray computed tomography for observing biological soft tissues. Nature Medicine, 2, 473–475, https://doi.org/10.1038/nm0496-473.

Moore, R.L., Patera, A., Bonnin, A., and Ménez, B. (2022) Grating-based X-ray computed tomography for improved contrast on a heterogeneous geomaterial. Frontiers in Earth Science, 10, 878738, https://doi.org/10.3389/feart.2022.878738.

Odedra, D., Narayanasamy, S., Sabongui, S., Priya, S., Krishna, S., and Sheikh, A. (2022) Dual energy CT physics—A primer for the emergency radiologist. Frontiers in Radiology, 2, 820430, https://doi.org/10.3389/fradi.2022.820430.

Pak, T., Archilha, N.L., Mantovani, I.F., Moreira, A.C., and Butler, I.B. (2019) An X-ray computed micro-tomography dataset for oil removal from carbonate porous media. Scientific Data, 6, 190004, https://doi.org/10.1038/sdata.2019.4.

Parisatto, M., Turina, A., Cruciani, G., Mancini, L., Peruzzo, L., and Cesare, B. (2018) Three-dimensional distribution of primary melt inclusions in garnets by X-ray microtomography. American Mineralogist, 103, 911–926, https://doi.org/10.2138/am-2018-6216.

Sagisaka, M., Toyoda, T., Kataoka, J., Arimoto, M., Kawashima, H., Kobayashi, S., Murakami, K., Okumura, K., Sato, D., Yoshiura, K., and others. (2023) Experiment of in vivo imaging with third generation setup using Photon-Counting CT with 64ch Multi-Pixel Photon Counter. Nuclear Instruments and Methods in Physics Research Section A: Accelerators, Spectrometers, Detectors and Associated Equipment, 1045, 167580, https://doi.org/10.1016/j.nima.2022.167580.

Sato, D., Arimoto, M., Yoshiura, K., Mizuno, T., Aiga, K., Ishiguro, K., Tomoda, T., Kawashima, H., Kobayashi, S., Okumura, K., and others. (2023) Initial results of in vivo CT imaging of contrast agents using MPPC-based photon-counting CT. Nuclear Instruments and Methods in Physics Research Section A: Accelerators, Spectrometers, Detectors and Associated Equipment, 1048, 167960, https://doi.org/10.1016/j.nima.2022.167960.

Schmidt, B. and Flohr, T. (2020) Principles and applications of dual source CT. Physica Medica, 79, 36–46, https://doi.org/10.1016/j.ejmp.2020.10.014.

Selem, A.M., Agenet, N., Gao, Y., Raeini, A.Q., Blunt, M.J., and Bijeljic, B. (2021) Pore-scale imaging and analysis of low salinity waterflooding in a heterogeneous carbonate rock at reservoir conditions. Scientific Reports, 11, 15063, https://doi.org/10.1038/s41598-021-94103-w.

Sellerer, T., Ehn, S., Mechlem, K., Duda, M., Epple, M., Noël, P.B., and Pfeiffer, F. (2019) Quantitative dual-energy micro-CT with a photon-counting detector for material science and non-destructive testing. PLoS One, 14, e0219659, https://doi.org/10.1371/journal.pone.0219659.

Sittner, J., Godinho, J.R.A., Renno, A.D., Cnudde, V., Boone, M., De Schryver, T., Van Loo, D., Merkulova, M., Roine, A., and Liipo, J. (2021) Spectral X-ray computed micro tomography: 3-dimensional chemical imaging. X-ray Spectrometry, 50, 92–105, https://doi.org/10.1002/xrs.3200.

Voltolini, M., Zandomeneghi, D., Mancini, L., and Polacci, M. (2011) Texture analysis of volcanic rock samples: Quantitative study of crystal and vesicles shape preferred orientation from X-ray microtomography data. Journal of Volcanology and Geothermal Research, 202, 83–95, https://doi.org/10.1016/j.jvolgeores.2011.02.003.

Willemink, M.J., Persson, M., Pourmorteza, A., Pelc, N.J., and Fleischmann, D. (2018) Photon-counting CT: Technical principles and clinical prospects. Radiology, 289, 293–312, https://doi.org/10.1148/radiol.2018172656.

Zandomeneghi, D., Voltolini, M., Mancini, L., Brun, F., and Polacci, M. (2010) Quantitative analysis of X-ray microtomography images of geomaterials: Application to volcanic rocks. Geosphere, 6, 793–804, https://doi.org/10.1130/GES00561.1.

Manuscript received June 15, 2023
Manuscript accepted January 5, 2024
Accepted manuscript online January 18, 2024
Manuscript handled by Don Baker

Endnote:

[1]Deposit item AM-24-99099. Online Materials are free to all readers. Go online, via the table of contents or article view, and find the tab or link for supplemental materials.